文章编号: 1001-9014(2025)05-0726-08

DOI:10. 11972/j. issn. 1001-9014. 2025. 05. 010

Noninvasive terahertz near-field nano-imaging of mouse embryonic fibroblasts

ZHONG Qin-Yang 1,2,3,4 , ZHANG Xiao-Qiu-Yan $^{1,4,5^*}$, WANG Ran 1,4 , ZHANG Tian-Yu 1,4,5 , TANG Fu 1,4,5 , JIANG Pei-Du $^{2,3^*}$, HU Min $^{1,4,5^*}$, LIU Sheng-Gang 1

- (1. Terahertz Research Center, School of Electronic Science and Engineering, University of Electronic Science and Technology of China, Chengdu 611731, China;
- 2. Department of Pharmacy, Personalized Drug Therapy Key Laboratory of Sichuan Province, Sichuan Provincial People's Hospital, University of Electronic Science and Technology of China, Chengdu 610072, China;
 - 3. School of Medicine, University of Electronic Science and Technology of China, Chengdu 610054, China;
 - 4. Key Laboratory of Terahertz Technology, Ministry of Education, Chengdu 611731, China;
 - 5. Tianfu Jiangxi Laboratory, Chengdu 641419, China)

Abstract: Fibroblasts support a broad range of essential organ functions via microarchitectural, biomechanical, and biochemical cues. Despite great advances in fluorescence, photoacoustic conversion, and Raman scattering over the past decades, their invasiveness and limited spatial resolution hinder the characterization of fibroblasts in a single cell. Here, taking mouse embryonic fibroblasts (MEFs) as an example, we propose a novel noninvasive approach to investigate the compositional distribution of MEFs at the single-cell scale via terahertz (THz) nanoscopy. Compared to the topological morphology, THz nano-imaging enables the component-based visualization of MEFs, such as the membrane, cytoplasm, nucleus, and extracellular vesicles (EVs). Notably, we demonstrate the real-space observation of the influence of rapamycin treatment on the increase of EVs in MEFs. Moreover, the line-cut and area-statistical analysis establishes the relationship between the topological morphology and the THz near-field amplitudes for different cellular components of MEFs. This work provides a new pathway to characterize the effects of pharmaceutical treatments, with potential applications in disease diagnosis and drug development.

Key words: fibroblasts, biomedical, terahertz, extracellular vesicles, nanoscopy

小鼠胚胎成纤维细胞的非侵入式太赫兹近场纳米成像

钟沁洋^{1,2,3,4}, 张晓秋艳^{1,4,5*}, 王 冉^{1,4}, 张天宇^{1,4,5}, 唐 福^{1,4,5}, 蒋培都^{2,3*}, 胡 旻^{1,4,5*}, 刘盛纲¹

(1. 电子科技大学 电子科学与工程学院 太赫兹科学技术研究中心, 四川 成都 611731;

- 2. 电子科技大学附属医院:四川省人民医院个体化药物治疗四川省重点实验室药学部,四川成都610072;
 - 3. 电子科技大学 医学院,四川 成都 610054;
 - 4. 太赫兹技术教育部重点实验室, 四川 成都 611731;
 - 5. 天府绛溪实验室,四川 成都 641419)

摘要:通过微结构、生物力学和生物化学等方式,成纤维细胞能够支持许多基本器官功能的实现。在过去几十年中,尽管荧光、光声转换和拉曼散射等技术取得了巨大进步,但它们的侵入性和有限的空间分辨率阻碍

Received date: 2025-01-09, revised date: 2025-03-26 收稿日期: 2025-01-09, 修回日期: 2025-03-26

Foundation items: Supported by the National Natural Science Foundation of China (61988102, 62401113, 92463308); the National Safety Academic Fund (U2130113); the Sichuan Science and Technology Program (2022JDJQ0065); the Chengdu Science and Technology Program (2024-YF05-01803-SN); the Sichuan Provincial Administration of Traditional Chinese Medicine (2024MS512) and the from Key Laboratory of THz Technology, Ministry of Education.

Biography: ZHONG Qin-Yang (1998-), female, Sichuan, master. Research area involves Terahertz biomedical imagings. E-mail: qinyangzhong1225@ 163. com.

^{*}Corresponding author: E-mail: zhang_xqy@uestc. edu. cn, peidujiang@uestc. edu. cn, hu_m@uestc. edu. cn

了成纤维细胞的单细胞表征。在这里,以小鼠胚胎成纤维细胞为例,基于太赫兹纳米显微镜提出了一种可以在单细胞尺度研究成纤维细胞成分分布的新方法。与表面形貌相比,太赫兹纳米成像可以实现小鼠胚胎成纤维细胞成分的可视化,如细胞膜、细胞质、细胞核和细胞外囊泡。值得注意的是,通过实空间方式观测了雷帕霉素处理对细胞外囊泡数量增加的影响。此外,截线和区域统计分析建立了不同细胞成分表面形貌和太赫兹近场幅值之间的对应关系。本工作为表征药物治疗效果提供了新途径,在疾病诊断和药物开发中具有潜在应用前景。

关键词:成纤维细胞;生物医学;太赫兹;细胞外囊泡;纳米显微镜

Introduction

Terahertz (THz) waves refer to a broad frequency range between 0.1-30 THz, corresponding to a wavelength between 10 and 3000 $\mu m^{[1]}$. In past decades, THz radiation has been widely used in scientific research and technical applications, such as telecommunications, security, and non-destructive imaging $^{[2\cdot3]}$. In these areas, the advantages of THz waves are mainly due to the low energy of THz photons, and multitudinous vibration and rotation frequencies are located in the THz range, indicating that THz techniques are suitable for noninvasive investigation and discrimination of various materials. Notably, milestones in the development of THz spectroscopy $^{[4\cdot6]}$ and THz imaging $^{[7\cdot8]}$ have boosted the evolution of THz techniques in material science $^{[9\cdot11]}$, molecular chemistry $^{[12]}$, and biomedical studies $^{[13\cdot15]}$.

Despite the THz techniques are extensively utilized in various scenes, the relatively low spatial resolution (~ 100 µm) severely restricts both fundamental and engineering applications^[16]. Although researchers have proposed several methods to break this limitation, for example, aperture-based THz near-field techniques, their highest spatial resolution is in the micrometer range [16-17]. Combined with the atomic force microscope (AFM), and THz systems based on different sources and detectors. THz nanoscopy could resolve the THz response of a sample under test at the nanoscale [16-19]. Since its development, THz nanoscopy has been broadly applied in condensed matter physics and material identifications, such as ultrafast charge carrier dynamics in semiconductors [20-24], polaritons in low-dimensional materials [25-27], and local permittivity of pigments [28] and dental caries [29-30]. Recently, several results of THz nanoscopy in biomedical research have opened new avenues for noninvasive characterization at the nanoscale[31-32], in which the heterogeneity and distribution of proteins^[33-34], bacteria^[35], viruses^[36], and cells^[37] can be well captured and analyzed.

Fibroblasts are one of the most common types to establish and maintain structural organization in several immune responses [38-39]. It is a malleable cell that enables altering its function and transforming into other cell types as required [40-44]. Despite the various optical methods that have been utilized for noninvasive imaging of fibroblasts, for example, fluorescence microscopy, second harmonic generation, optical coherence tomography, and photoacoustic microscopy, their current record spatial resolution is in the micrometer range [45-47]. Therefore, the cellular components of fibroblasts have not been well resolved at the single-cell scale, which is significant for fibroblast-

based cell development $^{[48\text{-}49]}$ and gene expression mechanisms $^{[50\text{-}51]}.$

To the best of our knowledge, the investigation and identification of fibroblasts by THz nanoscopy is still untouched. Here, we realize the noninvasive THz nearfield nano-imaging of the mouse embryonic fibroblast (MEFs) at the single-cell scale for the first time. We compared and analyzed the difference between the topological morphology (AFM) and THz near-field amplitude, the results indicate the ability of THz nanoscopy to observe the cellular components of MEFs. Notably, the number of EVs of MEFs in the experimental group is much higher than that in the control group, which means the rapamycin treatment may have positive effects on producing more EVs. Based on the line-cut and area-statistical analytics, we further reveal the discrepancy of the component-dependent THz near-field amplitudes in MEFs. These results provide a potential pathway to invasively study the compositional distribution and functionalities of fibroblasts including MEFs, at the nanoscale.

1 Methods

Cell preparation, fixation, and treatments. MEFs (purchased from ATCC) were cultured in high-glucose Dulbecco's modified Eagle's medium (Gibco) supplemented with 10% fetal bovine serum (Gibco), 100 U/mL penicillin, and 100 µg/mL streptomycin. Cells were incubated at 37 °C with 5% CO, saturation in a humid atmosphere. Highly doped silicon (from SurfaceNet LLC, $\rho \sim 0.136 \ \Omega \cdot \text{cm}$), which has broad biological adaptability and high near-field reflectivity, was chosen as the substrate. Cells were seeded onto the substrates and washed three times with phosphate buffer saline. The cells were fixed with anhydrous ethanol for 10 minutes. The cells were gently rinsed 3 times with ultrapure water and dried slowly at room temperature. For the experimental group, MEFs were treated with 20 ng/mL rapamycin for 24 h. The reason for treating MEFs with this concentration is based on our previous preliminary experiment to induce cell autophagy in MEFs and then increase the number of EVs. Similar treatment can be found in previous works^[52-53].

THz near-field nano-imaging. We use commercially available low-temperature grown GaAs photoconductive antennas (PCAs, Fraunhofer Heinrich Hertz Institute) as the emitter and detector to form a THz time-domain spectroscopy based on a commercially available system (TeraSmart, Menlo Systems GmbH). The PCA emits a broadband sub-picosecond pulse with frequencies from 0.1-3 THz. This pulse is coupled to a metallic AFM tip (Rocky Mountain Nanotechnology, LLC) of a

commercially available system (Neaspec GmbH, Attocube Systems AG). The light-matter interactions between the incident THz wave and the sample at the nanoscale are time-modulated when the AFM is in the tapping mode, and then scattered by the AFM tip in the far-field and finally detected by another PCA and demodulated into different harmonic orders through lock-in detection methods. In this experiment, we measure the peak amplitude of the scattered THz pulse and use it to realize high-fidelity THz near-field nano-imaging. The schematic of the THz near-field nano-imaging experiments on MEFs in this work is shown in Fig. 1(a), similar experimental set-ups can also be found in the work of previous authors [54-55].

2 Results and Discussion

We first verify the ability of THz near-field nano-imaging to map the cellular components of MEFs at the nanoscale, where the results for both the experimental and control groups are shown. As shown in Fig. 1 (b) and Fig. 1 (c), the curved surface is colored by the intensity of the second-order THz near-field amplitude (S2), while the height of this surface and the contour lines at the bottom indicate the topological morphology (AFM).

In Fig. 1(b) and Fig. 1(c), the cellular components of MEFs, such as the membrane, cytoplasm, and nucleus are well captured by THz near-field nano-imaging, where the S2 of MEFs for both the experimental and control groups is much lower than that of the THz reflective type substrate (highly doped silicon). It can be observed that the minimum values of S2 are concentrated in the central region of MEFs, corresponding to the position of the nucleus. Apart from these similar characteristics for both the experimental and control groups, we notice that the EVs are randomly distributed closely outside the MEF only for the experimental group (Fig. 1(b)). However, there is hardly any obvious feature of this in Fig. 1(c) for the control group.

To further compare the discrepancy between the MEFs of the experimental and control groups, and the relationship between the AFM and THz near-field amplitudes of the first, second, and third order (S1, S2, and S3), we randomly select two typical THz nano-imaging

results of MEF cells for the experimental and control groups respectively, which are shown in Figure 2.

As shown in Figure 2, the nanoscale morphology of MEFs can be clearly distinguished from both the AFM and THz near-field amplitudes. Compared with the AFM images, which are only related to the relative heights of MEF, different orders of THz near-field amplitudes for (S1, S2, and S3) provide high-fidelity nano-contrast revealing the cellular components of MEFs, including the nucleus, membrane, cytoplasm, and EVs. For example, the height of the nucleus is inhomogeneously distributed, e. g. Figure 2(m), which could lead to misunderstanding the exact size and composition of the nucleus. However, for the THz near-field nano-imaging, e.g. Figure 2(n), it could not only determine the profile of the nucleus but also visualize the cytoplasm attached to the nucleus (left side of the nucleus). The reason for these discrepancies is based on the light-matter interactions in the near-field. Compared with the effects of heights, the THz near-field amplitudes are strongly dependent on the electromagnetic properties of the sample, such as the permittivity function and the surface conductivity^[54-57].

Moreover, EVs are distributed outside the MEFs in both the experimental and control groups. However, the number of EVs in the experimental group (Fig. 2(b) and 2(f)) is much higher than that in the control group (Fig. 2(j) and 2(n)). In Fig. 2(i)-2(p), some EVs also appear in the MEFs of the control group, but the number of EVs here is much lower than that of the experimental group (Fig. 2(a)-2(h)). In the panels of Fig. 2(i)-2(1), some features originate from the uneven surface morphology of the silicon substrate, such as defects and impurities, and the sizes of these features are much smaller than the size of the EVs in Fig. 2(a)-2(h). Very few EVs can be observed within the scan range (40×40) μm^2) of the results of control group 2. Despite the signalto-noise ratios of S3 are apparently worse than those of S1 and S2, where the subtle near-field contrasts of the cellular components of MEFs are no longer observable, these results shown in Figure 2 unfold the remarkable ability of THz nanoscopy to characterize the cellular components of MEFs.

To interpret the qualitative discrepancy in the num-

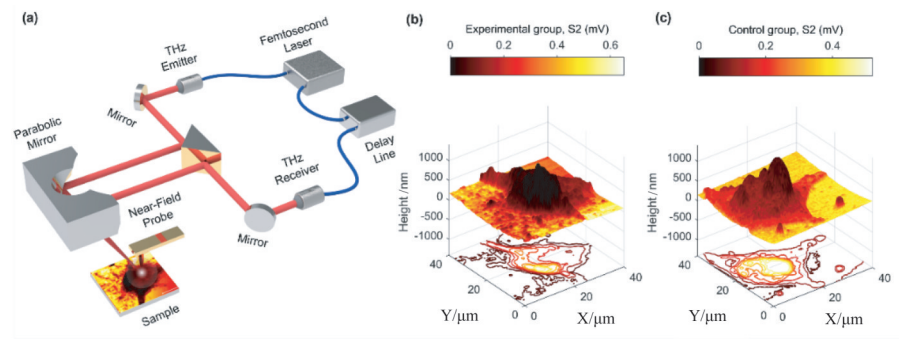


Fig. 1 Schematic of THz near-field nano-imaging experiments on MEFs.: (a) experimental set-up; (b,c) topological morphology (AFM) and second-order THz near-field amplitude (S2) of MEFs: (b) experimental group; (c) control group 图 1 小鼠胚胎成纤维细胞太赫兹近场纳米成像实验的示意图:(a)实验装置;(b,c)小鼠胚胎成纤维细胞的表面形貌和二阶太赫兹近场幅值成像结果: (b)实验组;(c)对照组

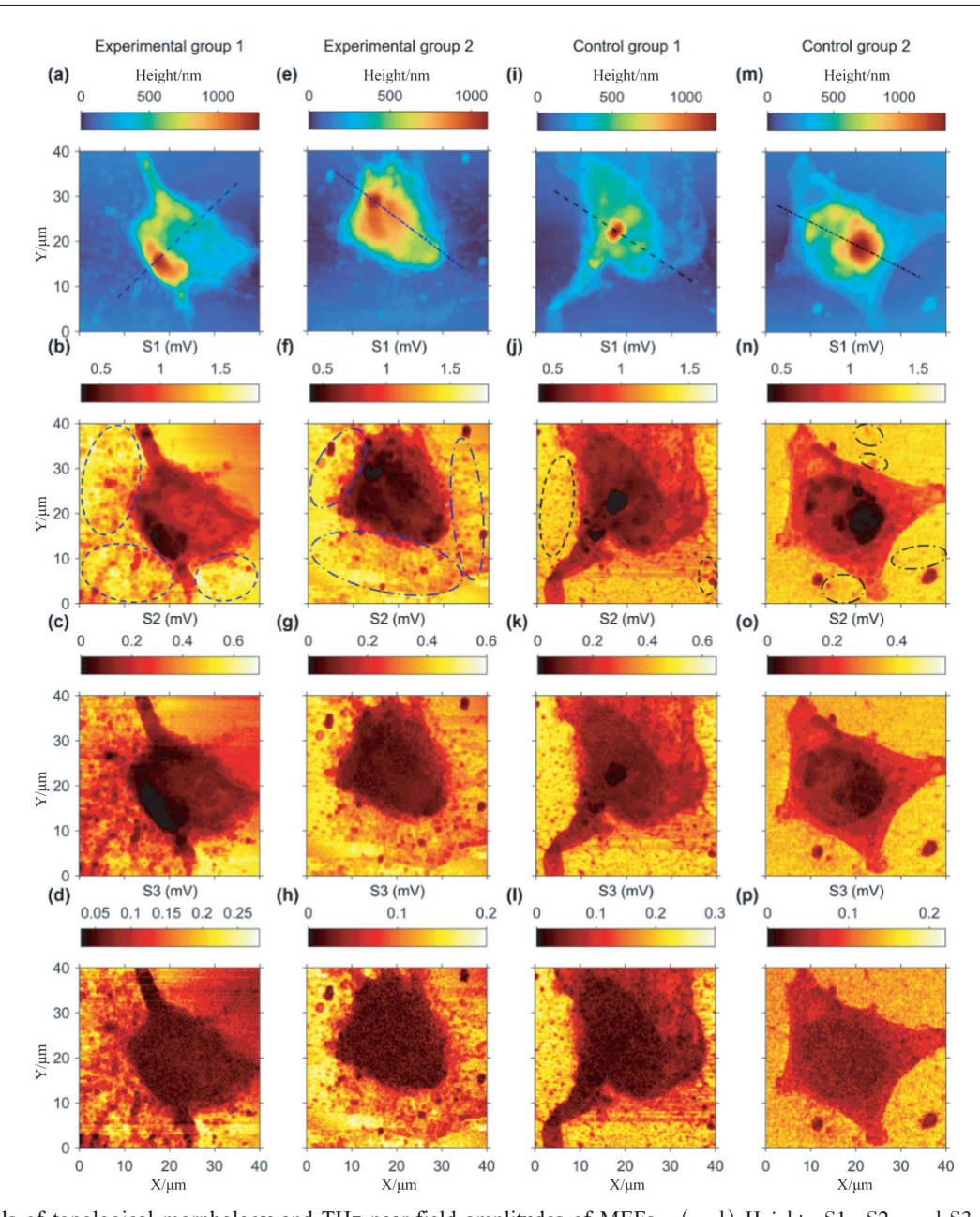


Fig. 2 Details of topological morphology and THz near-field amplitudes of MEFs. : (a-d) Height, S1, S2, and S3 of experimental group 1; (e-h) Height, S1, S2, and S3 of experimental group 2; (i-l) Height, S1, S2, and S3 of control group 1; (m-p) Height, S1, S2, and S3 of control group 2. (The marked line cuts in Figure 2(a), 2(e), 2(i), and 2(m) are used for line-cut analysis in Figure 3. The marked circles in Figure 2(b), 2(f), 2(j), and 2(n) indicate the position of EVs) 图 2 小鼠胚胎成纤维细胞表面形貌和太赫兹近场幅值成像图: (a-d) 实验组 1 的高度,一阶,二阶,三阶近场信号;(e-h) 实验组 2 的高度,一阶,二阶,三阶近场信号;(i-l) 对照组 1 的高度,一阶,二阶,三阶近场信号;(m-p) 对照组 2 的高度,一阶,二阶,三阶近场信号。图 2(a)、2(e)、2(i)和2(m)中标记出的虚线与图 3 中的线扫描分析相互对应。(图 2(b)、2(f)、2(j)和2(n)中标记出的圈形区域展示了细胞外囊泡所在的位置)

ber of EVs between the experimental and control groups, we would infer that the significant increase in the number of EVs in the rapamycin-treated MEFs is likely related to the inhibition of the mTORC1 pathway, which is known to modulate autophagy and cellular stress responses^[52-53]. By promoting autophagy and altering cellular metabolic states, rapamycin might drive cells to release more EVs as a mechanism to maintain intracellular homeostasis or improve intercellular communication. A similar role for mTORC1 also appears in exosome release, where the ra-

pamycin treatment significantly increased the number of exosomes, suggesting that mTORC1 inhibition delays senescence through increased release of exosomes^[59-60].

Next, we perform the line-cut (Figure 3) and areastatistical (Figure 4) analysis to establish the relationship between the topological morphology and THz near-field amplitudes and to obtain the correspondence of THz near-field amplitudes for different cellular components of MEFs. Figure 3 shows the line-cut profiles of AFM and THz near-field amplitudes of MEFs for the experimental

and control groups, respectively. These profiles capture information from the nucleus and cytoplasm of MEFs and correspond to the marked dashed and dot-dashed lines shown in Figure 2(a), 3(e), 3(i), and 3(m), respectively. The heights of MEFs, as shown in Figure 3(a), 3 (e), 3(i), and 3(m) are similar, suggesting comparable cellular morphology in terms of overall size and height. Compared with Figure 2, we can infer that the height ranges for the nucleus, cytoplasm, EVs, and substrate are approximately 800-1 300 nm, 400-800 nm, 200-400 nm, and 0-200 nm respectively. Moreover, the overall range of the near-field amplitudes is similar between the experimental and control groups (e.g., Figure 3(b), 3(f), 3(j), and 3(n)), reflecting consistent THz dielectric properties. These similarities indicate that the overall cellular morphology and THz electromagnetic properties of MEFs are preserved despite the rapamycin treatment.

As shown in Figure 3, the height and THz near-field amplitude are negatively correlated overall, with the higher part corresponding to a weaker near-field amplitude. For example, the values of S1 for the nucleus in all MEFs are around 0. 4-0. 6, while the values for the cytoplasm, EVs, and substrate are within the range of 0. 6-

1.0, 0.9-1.2, and 1.2-1.5, respectively. According to the principles of the tip-sample near-field responses in weakly absorbing samples [16-17,56-57], such as molecular materials and biomedical samples, the near-field amplitude of cellular components is approximatively proportional to their dielectric permittivity via the reflection coefficient. Moreover, a recent experimental work has proposed that the high cell nucleus density enhances the absorption and/or scattering of the THz waves^[58]. Therefore, we could infer that the THz permittivity of the nucleus is lower than that of the cytoplasm. Notably, we have also noticed that a recent work has established a systematic theoretical method to describe the THz near-field response of a complex morphological structure of protein based on the finite dipole model for multilayer samples [34], where the response depends on the thickness and permittivity of the sample, and the amplitude and distribution of the tiplocalized near-field. Therefore, more care should be taken to distinguish the contribution from different cellular components of MEFs.

Further, the response of EVs is also captured, e. g., sharp peaks in Figure 3(b) and 3(f). Although the height of EVs is small, which is buried in Figure 3(a) and 3(e), the corresponding response of THz near-field

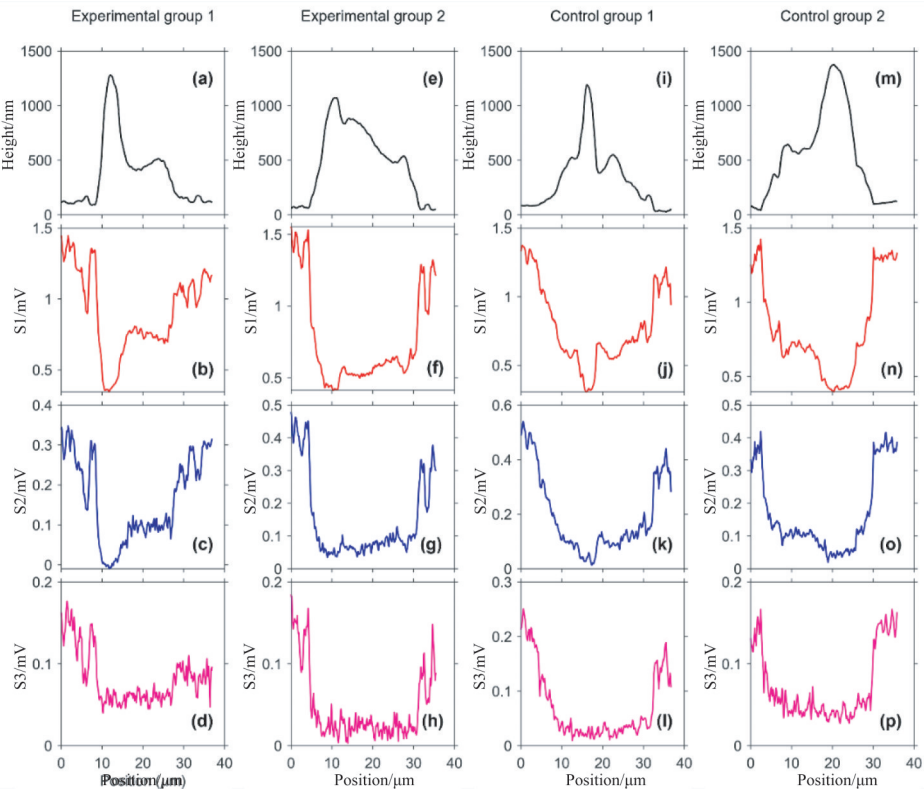


Fig. 3 Line-cut analysis of THz near-field amplitudes. :(a-d) Height, S1, S2, and S3 of experimental group 1(These data correspond to the blue dashed line marked in Figure 2(a)); (e-h) Height, S1, S2, and S3 of experimental group 2 (These data correspond to the blue dot-dashed line marked in Figure 2(e)); (i-l) Height, S1, S2, and S3 of control group 1 (These data correspond to the black dashed line marked in Figure 2(i)); (m-p) Height, S1, S2, and S3 of control group 2 (These data correspond to the black dot-dashed line marked in Figure 2(m))

图3 太赫兹近场幅值的线扫描分析: (a-d) 实验组1的高度,一阶,二阶,三阶近场信号(这些数据的取值位置对应图2(a)中的蓝色虚线); (e-h) 实验组2的高度,一阶,二阶,三阶近场信号(这些数据的取值位置对应图2(e)中的蓝色点划线); (i-l) 对照组1的高度,一阶,二阶,三阶近场信号(这些数据的取值位置对应图2(i)中的黑色虚线); (e-h) 对照组2的高度,一阶,二阶,三阶近场信号(这些数据的取值位置对应图2(m)中的黑色点划线)

amplitude is quite sharp from 1.2-1.5 of the substrate to 0.9-1.2 of the EVs (Figure 3(b)). These results indicate the ability of THz near-field nano-imaging to characterize MEFs based on near-field electromagnetic interactions in terms of the permittivity function. It is worth noting that only the combination of AFM and THz near-field amplitudes could provide an accurate description of cells at the nanoscale.

To further analyze the correlation between the heights and near-field amplitudes observed in Figure 3, without loss of generality, further area-statistical statistics were performed based on the data of experimental group 2 (Figure 2 (f) and 2 (g)) and control group 2 (Figure 2(n) and 2(o)), as shown in Figure 4. By combining the area-statistical statistics of the AFM height with the THz near-field amplitudes (S1 and S2), the relationship between the topological morphology and the near-field amplitude distribution is analyzed for both the experimental group (Fig. 4(a)) and the control group (Fig. 4 (b)). This approach allows a comprehensive comparison of the structural and dielectric properties between the two groups. In both groups, the near-field amplitudes (S1 and S2) exhibit an exponential decay with increasing heights, consistent with the near-field interaction model that is analyzed above. This trend highlights the expected physical correlation between the height of MEFs and the localized near-field amplitudes.

In the experimental group, most points are primarily located around 100 nm, with corresponding near-field amplitudes concentrated around 1.2-1.4 (S1) and 0.3-0.4 mV (S2), respectively. For the control group, the

near-field amplitudes are also concentrated around 1.25-1. 35 mV (S1) and 0. 32-0. 4 mV (S2) when the heights are around 200 nm. This region corresponds to the substrate. For the experimental group, another peak appears at lower near-field amplitudes 0.4-0.6 mV (S1) and 0.02-0.1 mV (S2), which mainly corresponds to the nucleus, while this feature is absent in the control group (Figure 4 (b)). We conclude that this difference depends on the depth of the nucleus. The entire nucleus is located at the top of the cell in experimental group 2 (Figure 2(f)), while the left part of the cell in control group 2 is covered by the overlying cytoplasm. These results indicate that the method proposed in this work, which is based on the combination of AFM and THz near-field nano-imaging, could be used to secure the morphology and components of MEFs.

3 Conclusions

In conclusion, we propose a novel pathway to investigate and distinguish a typical fibroblast, MEFs, in a non-destructive manner at the nanoscale using THz nanoscopy. Our methods and results reveal that the THz near-field nano-imaging has an outstanding ability to uncover the components and morphology of MEFs. We characterize the MEFs for both the experimental and control groups, using the number of randomly distributed EVs as the criterion for distinguishing these two types of MEFs. Looking ahead, the research of THz nanoscopy in biomedical and biological fields is promising but also challenging, especially for understanding and identifying

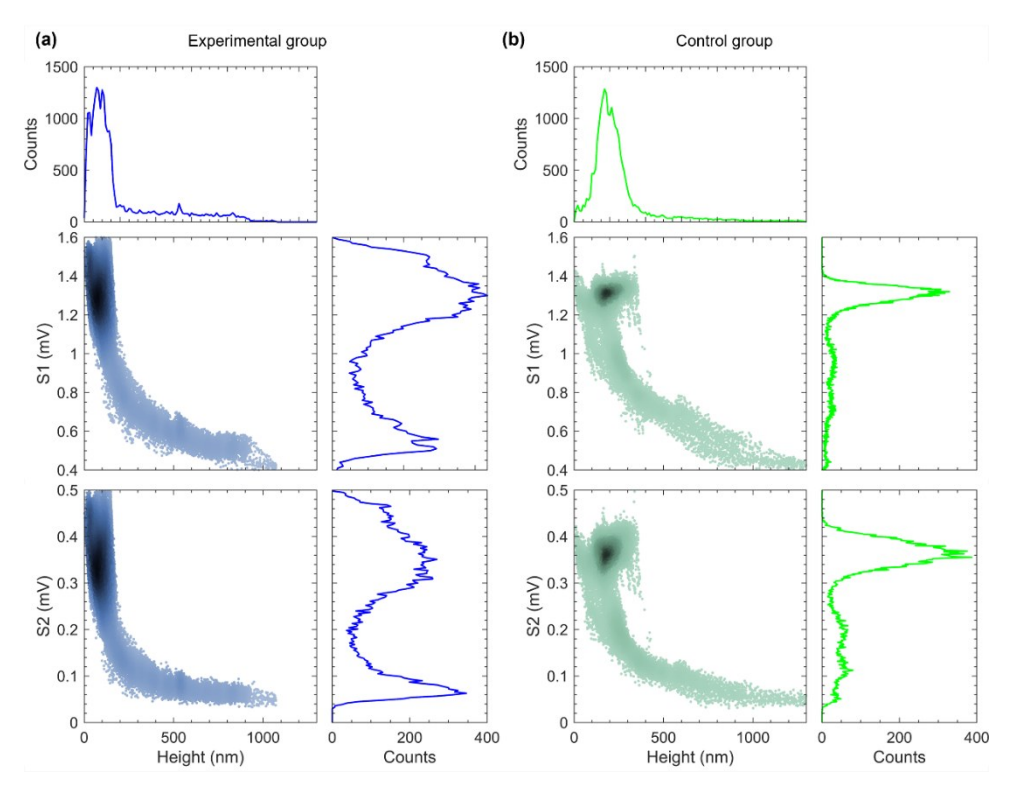


Fig. 4 Comparison of topological morphology and THz near-field amplitudes via area-statistical analysis: (a) experimental group; (b) control group.

图 4 通过区域统计方法分析对比表面形貌与太赫兹近场幅值:(a)实验组;(b)对照组

the bio-mechanisms at the nanoscale.

Acknowledgment

The authors acknowledged the support of Chengdu Miji Technology Co., Ltd. (MiJi).

References

- [1] Tonouchi M. Cutting-edge terahertz technology [J]. Nature Photonics, 2007, 1(2): 97–105.
- [2] Dhillon S S, Vitiello M S, Linfield E H, et al. The 2017 terahertz science and technology roadmap [J]. Journal of Physics D: Applied Physics, 2017, 50(4): 043001.
- [3] Leitenstorfer A, Moskalenko AS, Kampfrath T, et al. The 2023 terahertz science and technology roadmap[J]. Journal of Physics D: Applied Physics, 2023, 56(22): 223001.
- [4] Jepsen P U, Cooke D G, Koch M. Terahertz spectroscopy and imaging Modern techniques and applications [J]. Laser & Photonics Reviews, 2011, 5(1): 124–166.
- [5] Neu J, Schmuttenmaer C A. Tutorial: An introduction to terahertz time domain spectroscopy (THz-TDS)[J]. Journal of Applied Physics, 2018, 124(23): 231101.
- [6] Koch M, Mittleman D M, Ornik J, et al. Terahertz time-domain spectroscopy [J]. Nature Reviews Methods Primers, 2023, 3(1): 48.
- [7] Guerboukha H, Nallappan K, Skorobogatiy M. Toward real-time terahertz imaging [J]. Advances in Optics and Photonics, 2018, 10 (4): 843-938.
- [8] Li X, Li J, Li Y, et al. High-throughput terahertz imaging: progress and challenges [J]. Light: Science & Applications, 2023, 12 (1): 233.
- [9] Ulbricht R, Hendry E, Shan J, et al. Carrier dynamics in semiconductors studied with time-resolved terahertz spectroscopy [J]. Reviews of Modern Physics, 2011, 83(2): 543-586.
- [10] Kampfrath T, Tanaka K, Nelson K A. Resonant and nonresonant control over matter and light by intense terahertz transients [J]. Nature Photonics, 2013, 7(9): 680-690.
- [11] Yang C J, Li J, Fiebig M, et al. Terahertz control of many-body dynamics in quantum materials [J]. Nature Reviews Materials, 2023, 8 (8): 518-532
- [12] Choi W J, Lee S H, Park B C, et al. Terahertz circular dichroism spectroscopy of molecular assemblies and nanostructures [J]. Journal of the American Chemical Society, 2022, 144(50): 22789-22804.
- [13] Shi S, Yuan S, Zhou J, et al. Terahertz technology and its applications in head and neck diseases [J]. iScience, 2023, 26(7): 107060.
- [14] Chen X, Lindley-Hatcher H, Stantchev R I, et al. Terahertz (THz) biophotonics technology: Instrumentation, techniques, and biomedical applications [J]. Chemical Physics Reviews, 2022, 3 (1): 011311
- [15] Guo Y, Chen L, Yan S, et al. Current research status of terahertz biomedical applications [J]. Journal of Infrared and Millimeter Waves, 2024, 43(5): 642-656.
- [16] Cocker T L, Jelic V, Hillenbrand R, et al. Nanoscale terahertz scanning probe microscopy [J]. Nature Photonics, 2021, 15 (8): 558-569.
- [17] Guo X, Bertling K, Donose B C, et al. Terahertz nanoscopy: Advances, challenges, and the road ahead [J]. Applied Physics Reviews, 2024, 11(2): 021306.
- [18] Keilmann F, Hillenbrand R. Near-field microscopy by elastic light scattering from a tip[J]. Philosophical Transactions of the Royal Society of London. Series A: Mathematical, Physical and Engineering Sciences, 2004, 362(1817): 787-805.
- [19] Chen X, Hu D, Mescall R, et al. Modern scattering-type scanning near-field optical microscopy for advanced material research [J]. Advanced Materials, 2019, 31(24): 1804774.
- [20] Eisele M, Cocker T L, Huber M A, et al. Ultrafast multi-terahertz nano-spectroscopy with sub-cycle temporal resolution [J]. Nature Photonics, 2014, 8(11): 841-845.
- [21] Plankl M, Faria Junior P E, Mooshammer F, et al. Subcycle contact—free nanoscopy of ultrafast interlayer transport in atomically thin heterostructures [J]. Nature Photonics, 2021, 15(8): 594–600.
- [22] Siday T, Hayes J, Schiegl F, et al. All-optical subcycle microscopy on atomic length scales[J]. Nature, 2024, 629(8011): 329-334.
- [23] Zizlsperger M, Nerreter S, Yuan Q, et al. In situ nanoscopy of sin-

- gle-grain nanomorphology and ultrafast carrier dynamics in metal halide perovskites [J]. Nature Photonics, 2024, 18(9): 975–981.
- [24] Wang Y, Zhang T, Ma K, et al. Terahertz nanoscopy on low-dimensional materials: toward ultrafast physical phenomena [J]. ACS Applied Materials & Interfaces, 2025, 17(2): 2736-2755.
- [25] Alonso-González P, Nikitin A Y, Gao Y, et al. Acoustic terahertz graphene plasmons revealed by photocurrent nanoscopy [J]. Nature Nanotechnology, 2017, 12(1): 31–35.
- [26] Lundeberg M B, Gao Y, Asgari R, et al. Tuning quantum nonlocal effects in graphene plasmonics [J]. Science, 2017, 357 (6347): 187-191
- [27] Chen S, Leng P L, Konečná A, et al. Real-space observation of ultraconfined in-plane anisotropic acoustic terahertz plasmon polaritons [J]. Nature Materials, 2023, 22(7): 860-866.
- [28] Zhang X, Zhang X, Zhang Z, et al. Time-domain-filtered terahertz nanoscopy of intrinsic light-matter interactions [J]. Nano Letters, 2024, 24(47): 15008-15015.
- [29] Xiao F, Zhang X, Xu X, et al. Unveiling enamel demineralization mechanisms by sensitive dielectric differentiation based on terahertz nanospectroscopy [J]. Biomedical Optics Express, 2024, 15 (9): 5229-5237
- [30] Zhang A, Lei L, Cheng L, et al. Terahertz imaging detects oral cariogenic microbial domains characteristics [J]. Journal of Dental Research, 2024, 103(13): 1428-1436.
- [31] Hu X, Zhou L, Wu X, et al. Review on near-field detection technology in the biomedical field[J]. Advanced Photonics Nexus, 2023, 2 (4): 044002.
- [32] Yan S, Cheng G, Yang Z, et al. Terahertz scanning near-field optical microscopy for biomedical detection: Recent advances, challenges, and future perspectives [J]. Biotechnology Advances, 2025, 74: 108507.
- [33] Yang Z, Tang D, Hu J, et al. Near-field nanoscopic terahertz imaging of single proteins [J]. Small, 2021, 17(3): 2005814.
- [34] Yang Z, Li D, Chen L, et al. Near-field terahertz morphological reconstruction nanoscopy for subsurface imaging of protein layers [J]. ACS Nano, 2024, 18(14): 10104-10112.
- [35] Schäffer S, Wigger A K, Bolívar P H. Substrate-enhanced THz nanoscopic recognition of single bacteria [C]. In: 2019 44th International Conference on Infrared, Millimeter, and Terahertz Waves (IRMMW-THz), Paris: IEEE, 2019: 1-2.
- [36] Zhang X, Hu M, Zhao X, et al. Biomedical Applications of terahertz near-field imaging [C]. In: 2021 46th International Conference on Infrared, Millimeter and Terahertz Waves (IRMMW-THz), Chengdu: IEEE, 2021: 1–2.
- [37] Hu X, Zhang G, Qian J, et al. Terahertz s-SNOM imaging of a single cell with nanoscale resolution [J]. Nano Letters, 2024, 24(25): 7757-7763.
- [38] Plikus M V, Wang X, Sinha S, et al. Fibroblasts: Origins, definitions, and functions in health and disease [J]. Cell, 2021, 184 (15): 3852-3872.
- [39] Harding J, Vintersten-Nagy K, Yang H, et al. Immune-privileged tissues formed from immunologically cloaked mouse embryonic stem cells survive long term in allogeneic hosts[J]. Nature Biomedical Engineering, 2024, 8(4): 427-442.
- [40] Takahashi K, Yamanaka S. Induction of pluripotent stem cells from mouse embryonic and adult fibroblast cultures by defined factors [J]. Cell, 2006, 126(4): 663-676.
- [41] Efe J A, Hilcove S, Kim J, et al. Conversion of mouse fibroblasts into cardiomyocytes using a direct reprogramming strategy [J]. Nature Cell Biology, 2011, 13(3): 215-222.
- [42] Huang P, He Z, Ji S, et al. Induction of functional hepatocyte-like cells from mouse fibroblasts by defined factors [J]. Nature, 2011, 475(7356): 386-389.
- [43] Sekiya S, Suzuki A. Direct conversion of mouse fibroblasts to hepato-cyte-like cells by defined factors [J]. Nature, 2011, 475 (7356): 390-393.
- [44] Lalit P A, Rodriguez A M, Downs K M, et al. Generation of multipotent induced cardiac progenitor cells from mouse fibroblasts and potency testing in ex vivo mouse embryos [J]. Nature Protocols, 2017, 12(5): 1029-1054.
- [45] Nikolaev V V, Kistenev Y V, Kröger M, et al. Review of optical methods for noninvasive imaging of skin fibroblasts—From in vitro to ex vivo and in vivo visualization [J]. Journal of Biophotonics, 2024, 17(1): e202300223.
- [46] Lendahl U, Muhl L, Betsholtz C. Identification, discrimination and heterogeneity of fibroblasts [J]. Nature Communications, 2022, 13

- (1): 3409.
- [47] Chhabra Y, Weeraratna A T. Fibroblasts in cancer: Unity in heterogeneity[J]. Cell, 2023, 186(8): 1580-1609.
- [48] Bryja V, Bonilla S, Arenas E. Derivation of mouse embryonic stem cells[J]. Nature Protocols, 2006, 1(4): 2082-2087.
- [49] Sturmlechner I, Sine C C, Jeganathan K B, et al. Senescent cells limit p53 activity via multiple mechanisms to remain viable [J]. Nature Communications, 2022, 13(1): 3722.
- [50] Tian Q, Zhou L. Lactate activates germline and cleavage embryo genes in mouse embryonic stem cells[J]. Cells, 2022, 11(3): 548.
- [51] Singhal P K, Sassi S, Lan L, et al. Mouse embryonic fibroblasts exhibit extensive developmental and phenotypic diversity [J]. Proceedings of the National Academy of Sciences, 2016, 113(1): 122-127.
- [52] Zou W, Lai M, Jiang Y, et al. Exosome release delays senescence by disposing of obsolete biomolecules [J]. Advanced Science, 2023, 10(8): 2204826.
- [53] Kaeser-Pebernard S, Vionnet C, Mari M, et al. mTORC1 controls Golgi architecture and vesicle secretion by phosphorylation of SCYL1 [J]. Nature Communications, 2022, 13(1): 4685.
- [54] Stinson H T, Sternbach A, Najera O, et al. Imaging the nanoscale phase separation in vanadium dioxide thin films at terahertz frequen-

- cies [1]. Nature Communications, 2018, 9(1): 3604.
- [55] Jing R, Shao Y, Fei Z, et al. Terahertz response of monolayer and few-layer WTe2 at the nanoscale [J]. Nature Communications, 2021, 12(1): 5594.
- [56] Govyadinov A A, Amenabar I, Huth F, et al. Quantitative measurement of local infrared absorption and dielectric function with tip-enhanced near-field microscopy [J]. The Journal of Physical Chemistry Letters, 2013, 4(9): 1526-1531.
- [57] Mester L, Govyadinov A A, Chen S, et al. Subsurface chemical nanoidentification by nano-FTIR spectroscopy [J]. Nature Communications, 2020, 11(1): 3359.
- [58] Okada K, Serita K, Cassar Q, et al. Terahertz near-field microscopy of ductal carcinoma in situ (DCIS) of the breast[J]. Journal of Physics: Photonics, 2020, 2(4): 044008.
- [59] Foster K G, Fingar D C. Mammalian target of rapamycin (mTOR): conducting the cellular signaling symphony [J]. Journal of Biological Chemistry, 2010, 285(19): 14071-14077.
- [60] Zhang H, Shen Y, Kim I, et al. Electrical stimulation increases the secretion of cardioprotective extracellular vesicles from cardiac mesenchymal stem cells[J]. Cells, 2023, 12(6): 875.